Progress In Electromagnetics Research C, Vol. 135, 241–253, 2023

Optimization of Flux-Concentrating Consequent-Pole Permanent Magnet Fault Tolerant Vernier Rim-Driven Machine

Wangsong He, Jingwei Zhu*, Zhe Wang, Jiubo Yue, and Tianrui Zhao

Abstract—In view of the problems of excessive magnetic flux leakage of the traditional permanent magnet fault-tolerant vernier rim-driven machine, low utilization rate of permanent magnets, and high price of permanent magnet materials, this paper proposes a flux-concentrating consequent-pole permanent magnet fault-tolerant vernier rim-driven machine structure. Firstly, combined with the magnetic field modulation theory, the no-load air gap magnetic density of the machine is analyzed, and the working principle of the multi-harmonic operation of the machine is explained according to the harmonic analysis. Secondly, parametric modeling is used to screen the critical structural parameters that can significantly affect electromagnetic performance of the machine, and the response surface method and sensitivity analysis are used to rank the sensitivity of the critical parameters. Then, the high-sensitivity parameters are first subjected to multi-objective optimization, and then adjusted according to the low-sensitivity parameters. Finally, the air gap magnetic density, back-EMF, cogging torque, and permanent magnet numbers of the machine before and after optimization are compared and analyzed by finite element analysis. The results show that the flux-concentrating consequent-pole permanent magnet vernier rim-driven machine has higher torque density, less torque ripple, and higher utilization of permanent magnets.

1. INTRODUCTION

Under the global goal of "carbon peaking and carbon neutrality", ship power will gradually shift from mechanization to electrification. Rim-Driven Thruster (RDT) is a new type of electric propulsion device that integrates the machine body, propeller blades, and ducts, and eliminates the transmission shaft, mechanical seal, and machine cooling system [1, 2].

In recent years, the research of RDT has been paid attention by research institutions. The U.S. Navy proposed the Tango Bravo plan in the early 21st century regards RDT as the core technology for the development of a new generation of submarines [3–6]. The Netherlands and Germany have also proposed strategies to develop large permanent magnet machines and all-electric propulsion systems [7–9]. Although in China the research on RDT is relatively late, many substantive research progresses have been made in a short period of time [10–13].

At present, the built-in integrated machines of the rim-driven thruster machines are mainly brushless DC machines and permanent magnet synchronous machines. The brushless DC machines have the disadvantage of large output torque ripple. Although the traditional permanent magnet synchronous machine overcomes the shortcomings of large torque ripple, it has a large number of slots and permanent magnet poles, and torque output capacity is limited [14].

Compared with traditional permanent magnet machines, permanent magnet vernier machine belongs to the magnetic field modulation machine, which can generate more effective harmonics by sacrificing the fundamental wave through the magnetic field modulation, and multiple harmonics

Received 28 May 2023, Accepted 1 August 2023, Scheduled 11 August 2023
* Corresponding author: Jingwei Zhu (zjwdl@dlmu.edu.cn).
The authors are with the College of Marine Electrical Engineering, Dalian Maritime University, China.

participate in the electromagnetic energy conversion to contribute to the output torque and improve the torque output capability. In addition, the number of pole pairs of the stator and rotor of the permanent magnet vernier machine is different, similar to the upper and lower scales of the vernier card, and its electromagnetic torque is multiplied by the pole ratio (rotor pole number/stator pole number) on the basis of the traditional permanent magnet machine [15, 16]. Therefore, permanent magnet vernier machine has a higher torque density than the traditional permanent magnet machine under the same volume.

In addition, for the sake of operational safety, rim-driven thruster also needs certain fault-tolerant performance. A five-phase split tooth-type fault-tolerant vernier machine was proposed in [17]. The paper elaborated the design principles of a fault-tolerant permanent magnet vernier machine, including multi-phase single-layer concentrated winding design, slot-pole matching design, etc. to achieve physical, electrical, magnetic, and thermal isolation. The stator modular design can further improve physical and thermal isolation capabilities [18].

To sum up, permanent magnet fault-tolerant vernier machine can be applied to rim propulsion device to improve the efficiency and reliability of ship propulsion and reduce the cost. However, problems such as magnetic flux leakage between poles, low utilization rate of permanent magnets, and relatively large number of permanent magnets limit the development of permanent magnet fault-tolerant vernier machines in the field of rim electric direct drive [19–24].

In this paper, on the basis of the traditional permanent magnet fault-tolerant vernier rim-driven machine, a consequent-pole structure is introduced, which greatly reduces the number of permanent magnets. The permanent magnet fault-tolerant vernier rim-driven machine studied in this paper adopts a bearing-less design that integrates the machine and propeller, which weakens the problem of asymmetric axial magnetic field. At the same time, in order to ensure the torque output of the machine, the permanent magnet adopts a flux-concentrating array to reduce magnetic flux leakage between poles and improve the utilization rate of the permanent magnet.

2. MACHINE STRUCTURE AND WORKING PRINCIPLE

2.1. Machine Structure

The structure of the machine is shown in Figure 1. The permanent magnets are surface-mounted. The non-magnetic propeller is directly welded on the inner surface of the rotor, and the yoke of the stator and rotor is relatively thin. The stator adopts a modular structure, and the isolation teeth and armature teeth are arranged alternately and unevenly distributed. Two modulation poles are opened on each armature tooth to jointly modulate the air gap magnetic field. Single-layer concentrated winding is adopted, and the permanent magnet on the rotor adopts a consequent-pole structure. In order to weaken the impact of the reduction in the number of permanent magnets on the output capacity of the machine, Halbach array is introduced. The permanent magnets on both sides are magnetized

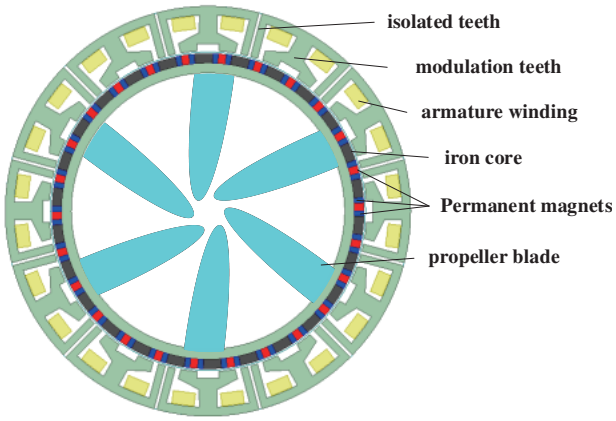

Figure 1. Structure of machine.

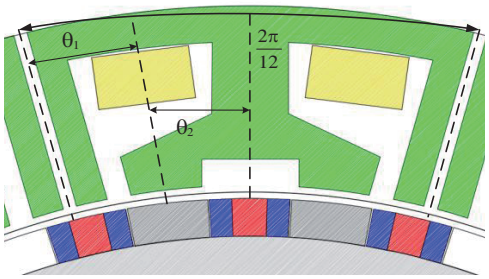

Figure 2. Enlarged view of teeth.

tangentially, and the permanent magnets in the middle are magnetized radially. This structure not only achieves the purpose of flux-concentration, but also effectively weakens oversaturation of the iron core. It is powered by an independent H-bridge inverter, which can realize phase-to-phase electrical isolation. The stator structure ensures that the machine has a large self-inductance and a strong ability to suppress short-circuit current, and the existence of isolated teeth can reduce the mutual inductance between poles, weakening the interference of the fault relative to the normal phase in the case of a fault.

2.2. Working Principle

In order to simplify the analysis, the flux-concentrating consequent-pole structure is regarded as a conventional consequent-pole structure. The expansion formula of the magnetomotive force generated by the consequent-pole permanent magnet is as follows:

$$F(\theta,t) = F_0 + \sum_{n=1,2,3,\ldots}^{\infty} F_m \cos\left[nP_r(\theta-\omega_r t)\right] \tag{1}$$

$$F_o = \frac{\alpha B_r h_m}{\mu_o \mu_r} \tag{2}$$

$$F_m = \frac{2B_r h_m}{n\pi\mu_o\mu_r}\sin(\alpha n\pi) \tag{3}$$

where P_r is the rotor pairs, B_r the residual magnetism of the permanent magnet, h_m the thickness of the permanent magnet, μ_o the vacuum permeability, μ_r the magnetic permeability of the permanent magnet, α the pole arc, and θ the relative angular position of the stator.

The magnetomotive force of the surface-mounted permanent magnet is positive and negative alternately. The magnetomotive force of the consequent-pole has only one-way amplitude, so the Fourier expansion of the magnetomotive force contains even harmonic components.

As shown in Figure 2, the armature teeth and isolation teeth are arranged alternately on the circumference, both of which participate in the magnetic field modulation, and the equivalent air gap permeance can be expressed as:

$$\Lambda(\theta) = \Lambda_o + \sum_{i=1,2,3,\ldots}^{\infty} \Lambda_i \cos(iZ_s\theta) \tag{4}$$

where Λ_o is the constant term of air gap permeance function, Λ_i the amplitude of air gap permeance function, and Z_s the number of modulation modules.

Taking the circumference span of an armature tooth and an isolation tooth as the period, the permeance distribution model can be divided into uniform distribution ($\theta_1 = \theta_2$) and nonuniform distribution ($\theta_1 \neq \theta_2$). Under the two structures, the permeance distribution is shown in Figure 3.

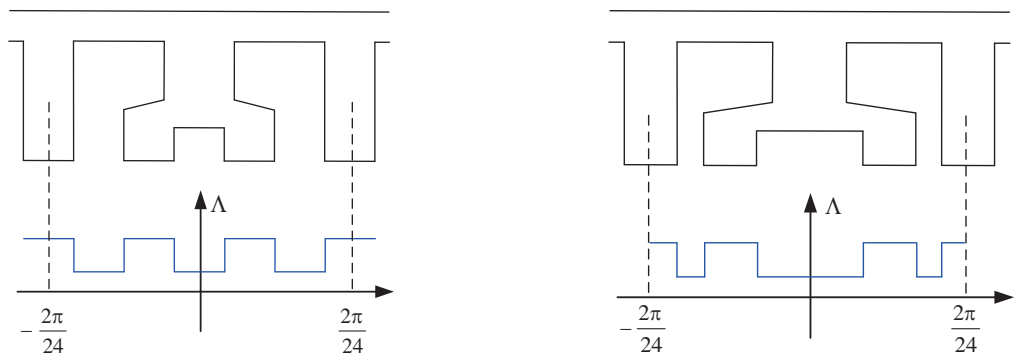

(a) Evenly distributed (b) Uneven distribution

Figure 3. Air gap magnetic conductivity model.

The period of uniformly distributed air gap permeance is three times of that of non-uniformly distributed air gap permeance, which can theoretically modulate more harmonics. According to Ohm's law of magnetic circuit, no-load air gap magnetic density can be obtained:

$$B(\theta,t) = F(\theta,t)\Lambda(\theta) \approx F_o\Lambda_o + F_m\Lambda_o\cos\left[P_r(\theta-\omega_r t)\right] + F_o\sum_{i=1,2,3,\ldots}^{\infty}\Lambda_i\cos(iZ_s\theta)$$
$$+\frac{1}{2}\sum_{i=1,2,3,\ldots}^{\infty}\cos(P_r\theta+iZ_s\theta-P_r\omega_r t)+\frac{1}{2}\sum_{i=1,2,3,\ldots}^{\infty}\cos(P_r\theta-iZ_s\theta-P_r\omega_r t) \quad (5)$$

The frequency of air gap magnetic density harmonics during no-load operation mainly includes P_r, $|P_r - iZ_s|$, $P_r + iZ_s$, $i = 1, 2, 3, \ldots$. As shown in Figure 4, fast Fourier transform (FFT) analysis of no-load air gap can be obtained. According to the Ampere's law of current, the harmonic magnetic electromotive force formula for a six phase concentrated winding can be obtained:

$$\begin{cases} F_A = F\cos v\theta\cos\omega t \\ F_B = F\cos v\left(\theta-\dfrac{2\pi}{3}\right)\cos\left(\omega t+\dfrac{2\pi}{3}\right) \\ F_C = F\cos v\left(\theta+\dfrac{2\pi}{3}\right)\cos\left(\omega t-\dfrac{2\pi}{3}\right) \\ F_U = F\cos v\left(\theta-\dfrac{\pi}{6}\right)\cos\left(\omega t-\dfrac{\pi}{3}\right) \\ F_V = F\cos v\left(\theta-\dfrac{5\pi}{6}\right)\cos\left(\omega t+\dfrac{\pi}{3}\right) \\ F_W = F\cos v\left(\theta+\dfrac{\pi}{2}\right)\cos\left(\omega t-\pi\right) \end{cases} \quad (6)$$

where F is the amplitude of the harmonic magnetomotive force, v the harmonic order, θ the mechanical angle from the A-phase winding axis, and ω the electrical angular velocity of the passing current. Six-phase synthetic magnetomotive force F^* can be obtained:

$$F^* = F_A + F_B + F_C + F_U + F_V + F_W \quad (7)$$

When $v = 3k, k,\ k = 1, 2, 3, \ldots,\ F^* = 0$, the winding magnetomotive force does not contain the $3k$th and $4k$th magnet flux harmonics. Two sets of windings with a mechanical angle difference of 180° are connected in positive phase to eliminate odd harmonics. When the winding is excited independently, the harmonic analysis of air gap magnetic density is shown in Figure 5.

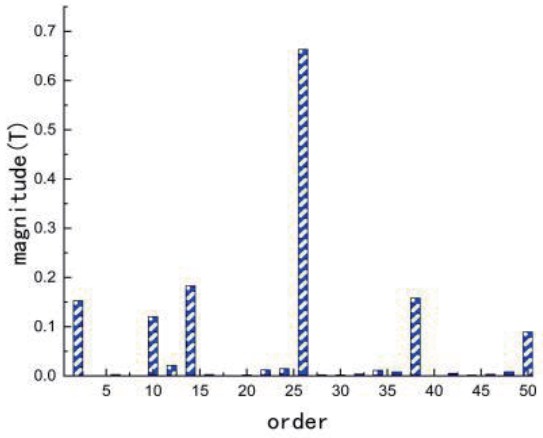

Figure 4. PM harmonic.

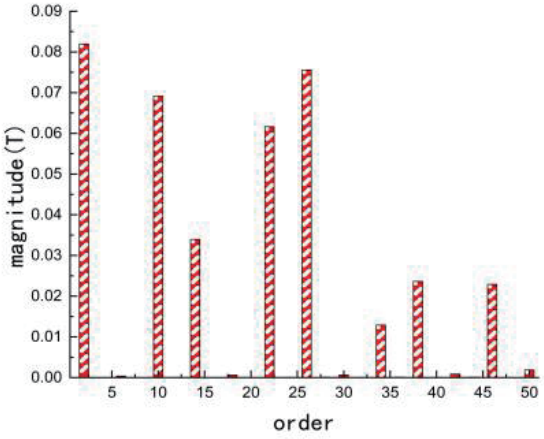

Figure 5. Armature winding harmonic.

According to the working principle of multiple harmonics, the air gap magnetic density of permanent magnet and winding air gap magnetic density correspond to the same frequency, rotation direction, and speed, which can be coupled to produce stable electromagnetic torque, improve the output capacity of the machine torque, and the content of unnecessary harmonics is less, which is conducive to the suppression of torque ripple.

3. HIGH DIMENSIONAL MULTI-OBJECTIVE OPTIMIZATION

3.1. Selection of Optimization Parameters and Optimization Objectives

The redundancy capacity of the six-phase machine is strong, which is beneficial for improving the fault tolerance performance. Fractional slot concentrated winding can realize electromagnetic isolation between phases and has good fault-isolation ability. The stator size, rotor size, winding turns, and axial length involve the calculation of electro-mechanical load and magnetic load, so the performance matching should be considered. Therefore, the number of machine phases, slots, stator inner and outer diameters, rotor inner and outer diameters, winding turns, axial length, and slot pole fit are not considered as optimization variables.

Polar arc and permanent magnet height, as the key parameters affecting the distribution of air gap magnetomotive force, affect the output capacity of machine torque through affecting the no-load back-EMF. As the main carrier of magnetic field modulation, the modulator teeth can sacrifice the fundamental wave to modulate rich working harmonics and produce larger output torque. In addition, the modulation teeth can provide a more abundant choice of magnetic circuit, which can improve the density distribution. Isolation teeth provide physical isolation between windings and can greatly weaken the fault relative to the normal phase interference. The modular design of the stator achieves phase-to-phase magnetic isolation by embedding air slots in the isolation teeth, which can also reduce the stator iron consumption to a certain extent, but the air slots also produce torque ripple.

In summary, the polar arc α, permanent magnet height h_m, modulating tooth height h, modulating tooth width f_h, isolating tooth width f_s, and stator air gap width h_g are selected as the optimization parameters, and the optimization objectives are to maximize the average torque and minimize the torque ripple. The optimization parameters are shown in Figure 6. Isolation tooth width f_s, polar arc α in consequent-polar structure, and torque ripple are defined as follows:

$$f_s = \frac{f_g}{f} \tag{8}$$

where f_g is the arc length of isolation tooth, and f is arc length between two isolation teeth.

$$\alpha = \frac{l_{pm}}{\tau} \tag{9}$$

$$\tau = l_{pm} + l_{Fe} \tag{10}$$

where l_{pm} is the arc length of permanent magnet, l_{Fe} the arc length of the iron core, and τ the pole pitch.

$$T_r = \frac{T_{pk2pk}}{T_{avg}} = \frac{T_{\max} - T_{\min}}{T_{avg}} \tag{11}$$

where T_{pk2pk} is the output torque peak-peak, and T_{avg} is the mean torque.

3.2. Optimization Idea

In the optimization of traditional permanent magnet fault-tolerant vernier rim machine, when the optimization parameters and optimization objectives are few, the sample database can be established by parameter sampling, and the response surface of the machine can be fitted out for multi-objective optimization. However, this paper has six optimization parameters and two optimization objectives. If the traditional multi-objective optimization method is adopted, it needs to first find an appropriate sampling strategy to ensure the scientific and reasonable selection of sample points; secondly, it needs to build a large set of sample data through simulation to ensure the accuracy of the response surface;

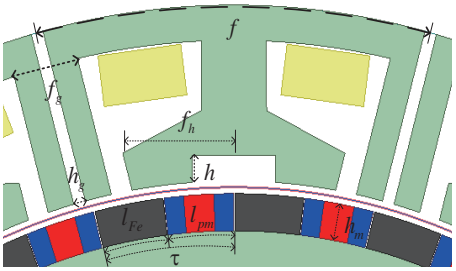

Figure 6. Optimization parameter.

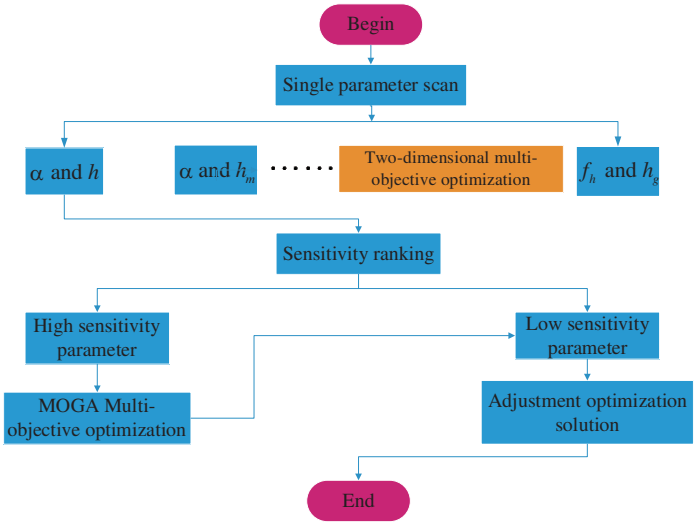

Figure 7. Optimization flow chart.

finally, it also needs to rely on the multi-objective optimization algorithm to iterate the optimal solution among the six structural parameters.

For high-dimensional multi-objective optimization, with the increase of the objective dimension, the number of non-dominant solutions is much larger than the number of candidate solutions, and the algorithm cannot take into account convergence and diversity in several iterations to select candidate solutions. Moreover, the performance evaluation index designed for multi-objective optimization problem is difficult to extend to high dimensional space. Therefore, if the traditional optimization approach is still adopted for the high-dimensional multi-objective optimization problem, the amount of computation and simulation period will increase exponentially.

To sum up, this section adopts the idea of descending order to simplify the high-dimension multi-objective optimization problems into multiple low-dimension multi-objective optimization problems. The specific optimization idea is as follows: First, the optimization range of structural parameters is determined by single parameter optimization method without considering the coupling between parameters, so as to reduce the calculation amount for subsequent optimization, and at the same time, the influence law of the parameter on electromagnetic performance can be obtained. Secondly, the six parameters are combined, a total of 15 (C_6^2) combination schemes. Then, based on optiSLang, the sensitivity analysis of each pair of parameters was carried out to obtain the sensitivity index of parameters to average torque and torque ripple, respectively. Combined with the results of sensitivity analysis, sensitivity ranking of the six parameters was conducted. Finally, the structural parameters with high sensitivity were selected for multi-objective optimization, and the optimal sample points were selected from the candidate solution set through the fine-tuning of structural parameters with low sensitivity to complete the final optimization. The high-dimensional multi-objective optimization process is shown in Figure 7.

3.3. Machine Parameter Optimization

According to the single parameter scanning results, the value ranges of six optimization parameters are shown in Table 1.

3.3.1. Establishment of Sample Database

Within the optimization range of Table 1, some groups of sample data are randomly sampled using Latin hypercube. In the value range of sparse samples, some sample points are added by Latin hypercube optimized by max-min method, which makes the sample distribution more reasonable and even.

Table 1. Parameter optimization range.

	h_m/mm	h/mm	f_h/mm	h_g/mm	α	f_s
Upper limit of optimization	7.5	7	10	2.2	0.98	0.22
Lower limit of optimization	6	3	7	1.8	0.88	0.18

Latin hypercube sampling is essentially a stratified sampling, that is, sampling is approximately completed from multivariate parameter distribution. However, common Latin hypercube sampling has the problem of uneven local distribution. In order to fill the whole space with discrete sample points as far as possible, it is necessary to add some sample points in the space with sparse sample points. According to the optimized Latin hypercube sampling based on the max-min method, the principle formula is as follows:

$$d_{ij} = \sqrt{(x_i - x_j)^2 + (y_i - y_j)^2} \quad i, j \in (1, n) \quad i \neq j \tag{12}$$

$$D_i = \min(d_{i1}, d_{i2}, \ldots, d_{in}) \tag{13}$$

In the formula, d_{ij} represents the distance between sample point i and sample point j; D_i is the eigenvalue of sample point i and represents the minimum distance from other sample points. Sample data are shown in Table 2.

Table 2. Preliminary optimization.

Parameter	Optimization	Adjustment
h_m/mm	8	6
α	0.85	0.89
f_h/mm	8	8.2
h/mm	5	5
f_s	0.22	0.22
h_g/mm	1.8	1.8
T_{avg}/Nm	29.13	32.22
T_r/%	2.59	2.32

3.3.2. Sensitivity Analysis

Within the selected optimization range, the sensitivity analysis was carried out for the six optimization parameters. The sensitivity index represents the correlation between the parameter and the optimization objective. The large/small sensitivity index indicates the strong/weak correlation degree, and the positive/negative sensitivity index indicates the change trend of the optimization objective with the parameter. Some of the results are shown in the Figure 8.

By analyzing parameter sensitivity, it can be found that the thickness of permanent magnet h_m, as a key parameter affecting the magnetic density distribution of the air gap, has a great influence on the average torque and torque ripple. The stator air gap h_g introduced by stator modularization has little influence on the torque performance. By comparing the remaining four optimization parameters, it can be found that the greater the impact of parameters is on the average torque, the smaller the impact is on torque ripple. The ranking of parameter sensitivity is shown in Figure 9.

3.3.3. Multi-Objective Optimization of Highly Sensitive Parameters

According to the ranking of sensitivity, the permanent magnet thickness h_m, pole arc α, and modulation tooth height f_h are firstly selected for multi-objective optimization. Then, according to the single-parameter scanning rule, in the solution set of candidate points, fine-tuning is carried out by modulating tooth height h, isolated tooth width f_s, and stator air gap h_x to complete the final optimization.

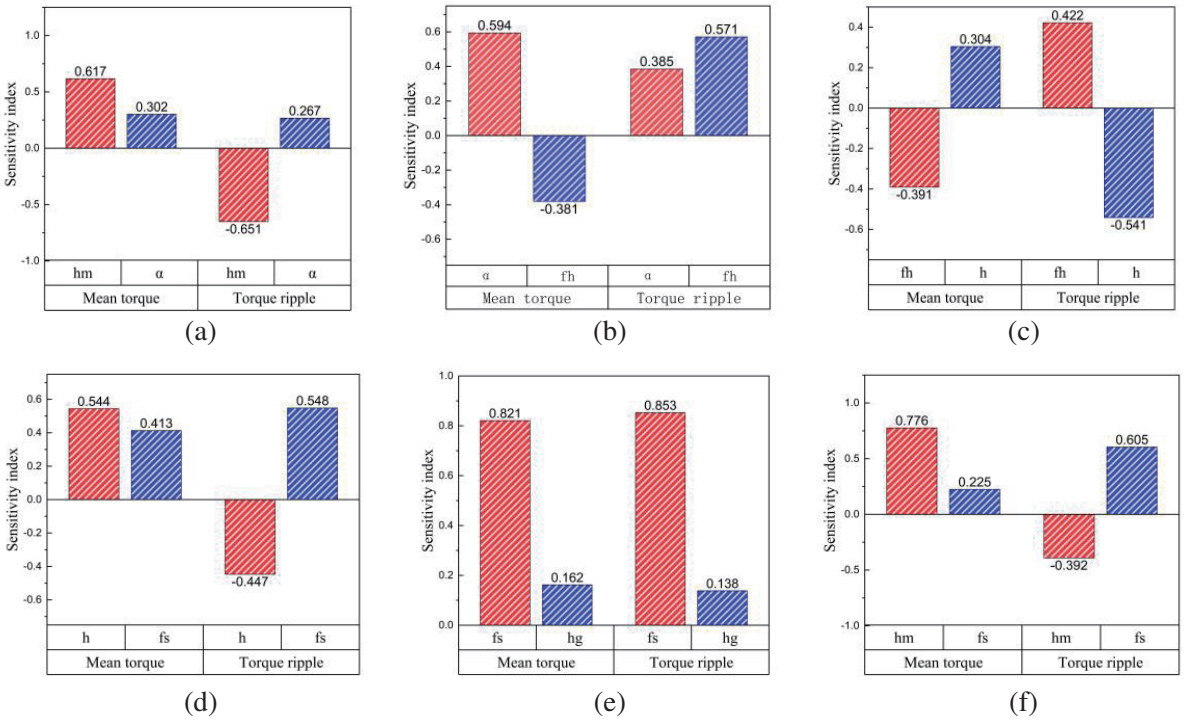

Figure 8. Sensitivity analysis.

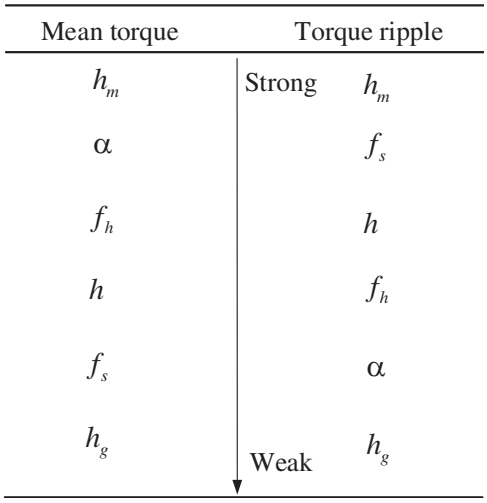

Figure 9. Sensitivity ranking.

In this experiment, the Kriging model with its own interpolation was selected to establish the response surface. Based on Kriging model with interpolation, the response of unknown points is predicted by known points to achieve unbiased estimation. There is little demand for initial samples. Moreover, the efficiency of adding points is high, and the global optimal solution can be obtained quickly. Then according to the multi-objective genetic algorithm MOGA, the optimal solution of key parameters was found. The MOGA algorithm can be divided into population initialization, fast non-dominated sorting, crowding allocation, tournament selection, and elite retention strategy. After multi-objective optimization, the key parameters and torque parameters of the machine are shown in Table 2.

After multi-objective optimization, the average torque is increased by about 10.6%, and the torque ripple is reduced by about 10.4%, which not only improves the torque output capacity but also weakens the torque ripple to a certain extent.

Finally, the low sensitive parameter modulation tooth height, isolation tooth width, and stator air gap are also taken into account, and appropriate parameters are selected in the optimal solution set to further reduce the torque ripple. The adjusted machine parameters are shown in Table 3.

Table 3. Final optimization.

Parameter	Optimization	Adjustment
h_m/mm	6	6
α	0.89	0.89
f_h/mm	8.2	8.2
h/mm	5	6
f_s	0.22	0.21
h_g/mm	1.8	1.9
T_{avg}/Nm	32.22	32.25
T_r/%	2.32	1.81

After the adjustment of low sensitivity parameters, the average torque remained basically unchanged, while the torque ripple was further suppressed. After the whole optimization process is completed, the average torque increase is about 10.7%, and the torque ripple is reduced by about 30.1%. For the whole optimization process, the torque waveform is shown in Figure 10.

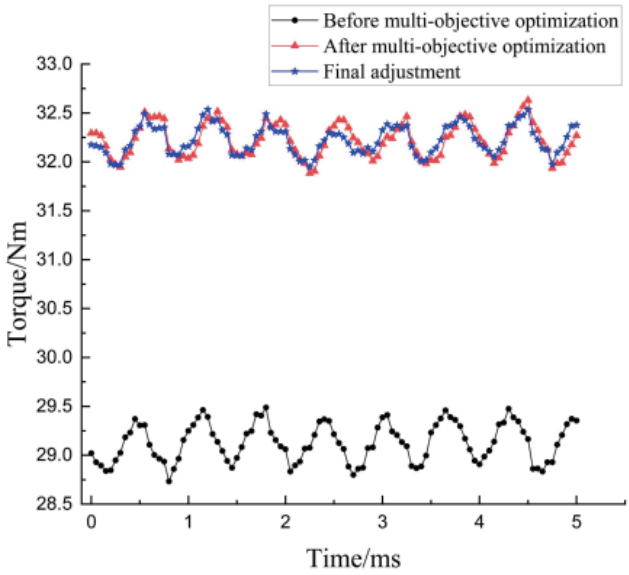

Figure 10. Torque comparison.

4. PERFORMANCE COMPARISON

In order to prove the effectiveness of the new structure, the parameters of the surface-mounted structure and the new structure are basically consistent, and the specific parameters are shown in Table 4.

Table 4. Machine parameter.

Parameter	Value	Parameter	Value
Rated power/kW	2.1	Rotor inner diameter/mm	172
Phase current/A	2.8	Air gap length/mm	2
Rated speed/rpm	600	Axial length/mm	45
Average torque/Nm	$\geqslant 25$	PM material	N38UH
Phase number	6	α	0.89
Stator slots	24	h_m/mm	6
Number of pole-pair	26	f_h/mm	8.2
Stator outside diameter/mm	255	h/mm	6
Stator inner diameter/mm	200	f_s	0.21
Rotor outside diameter/mm	196	h_g/mm	1.9

4.1. No-Load Performance

As shown in Figure 11, the number of peaks and troughs of air gap magnetic density is 26, which is consistent with the pole pairs of rotor. Moreover, the amplitude of air gap magnetic density peaks and troughs increases slightly after optimization. The order of air gap harmonics is mainly 26th, 2th, 10th, 14th, 38th, and 50th. These harmonic components work together to contribute to the output torque, and the amplitudes of effective harmonics increase slightly after optimization.

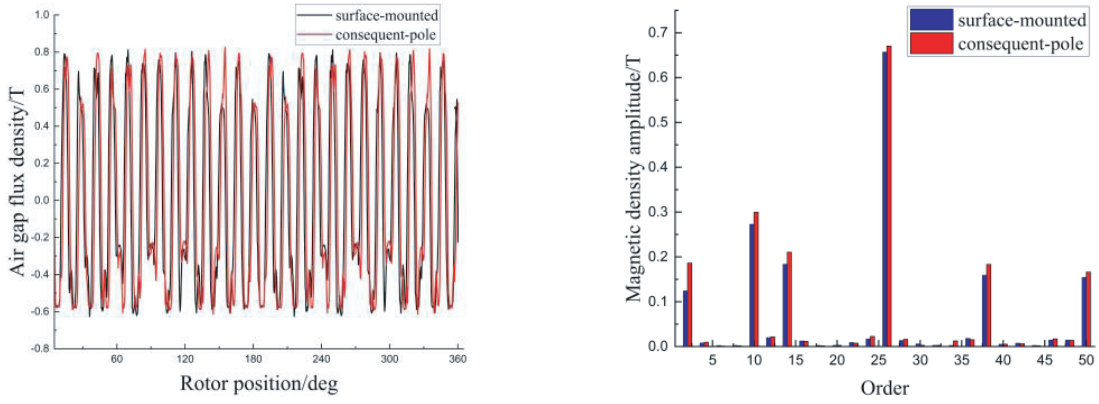

(a) air gap flux density (b) FFT analysis

Figure 11. Comparison of no-load air gap flux density.

As shown in Figure 12, after optimization, the no-load Back-EMF amplitude increases from 152 V to 165 V, increasing by about 8.6%. The harmonic analysis shows that the number of main harmonics in the Back-EMF is 1th, 2th, and 3th. Because the structure of consequent-pole is adopted, and the winding harmonic also contains the second harmonic, the Back-EMF also contains a small amount of the 2th harmonic.

4.2. Load Performance

As shown in Figure 13, under normal load, the overall magnetic density of the machine is less than 1.92 T. There is obvious saturation in stator yoke and rotor yoke before optimization, and the saturation phenomenon is obviously improved after optimization.

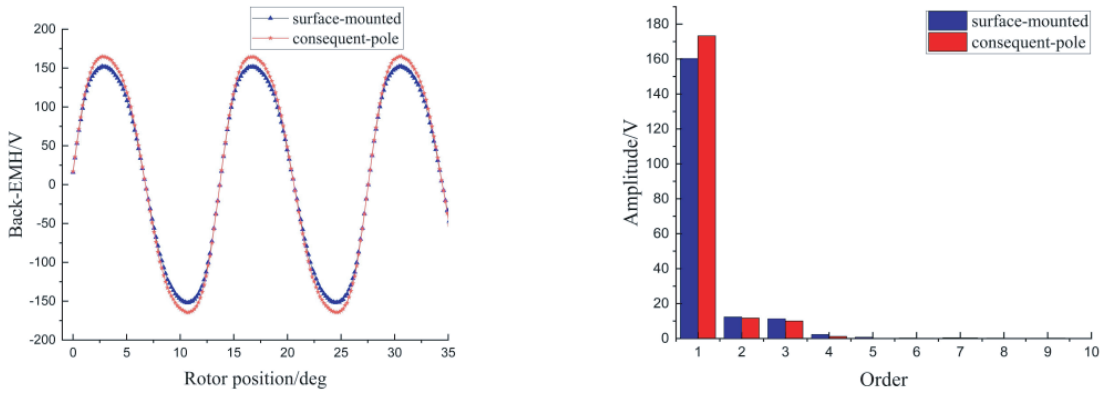

(a) No-load Back-EMF (b) FFT analysis

Figure 12. Comparison of no-load Back-EMF.

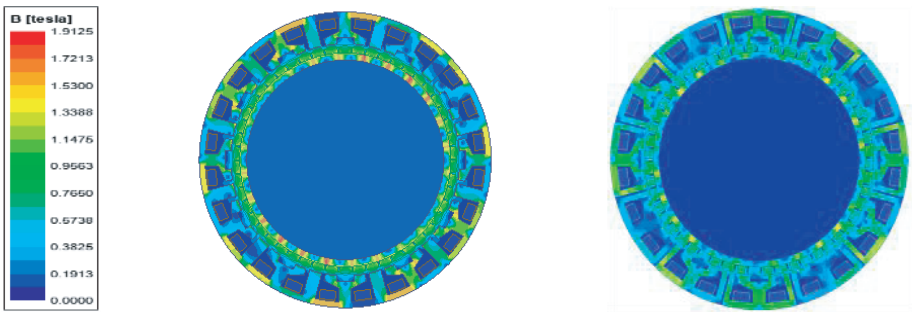

(a) surface-mounted (b) consequent-pole

Figure 13. Magnetic dense cloud map comparison.

As shown in Figure 14, the output torque of the traditional surface-mounted machine is about 26.5 Nm, and the torque ripple is about 5.98%, while the output torque of the flux-concentrating consequent-pole machine is about 32.3 Nm, and the torque ripple is about 1.81%. The torque of the new structure is increased by about 21.9%, and the torque ripple is reduced by about 63.1%.

The cogging torque is generated by the interaction between permanent magnet and stator tooth, and the cogging torque in no-load condition is the main component causing the torque ripple. As shown in Figure 15, compared with the surface-mounted, the cogging torque amplitude of the new structure decreases from 278.1 mNm to 169.4 mNm, and the cogging torque is reduced by 39.1%.

As shown in Table 5, the number of permanent magnets with flux-concentrating consequent-pole structure is 79.56 cm^3, while that with traditional surface-mounted is 180.18 cm^3. Combined with the performance comparison, the consumption of permanent magnets of the new structure is reduced by about 55.8%, which reduces the cost and improves the utilization rate of permanent magnets.

Table 5. Number of permanent magnets (PMs).

	Volume of a single PM/cm^3	Number of PMs	Volume of PMs/cm^3
Surface-mounted	3.465	52	180.18
Consequent-pole	3.06	26	79.56

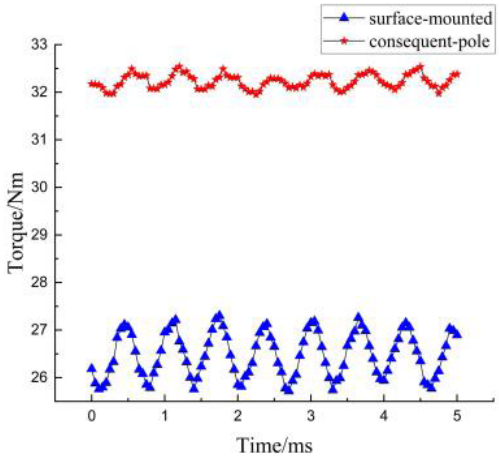

Figure 14. Comparison of output torque.

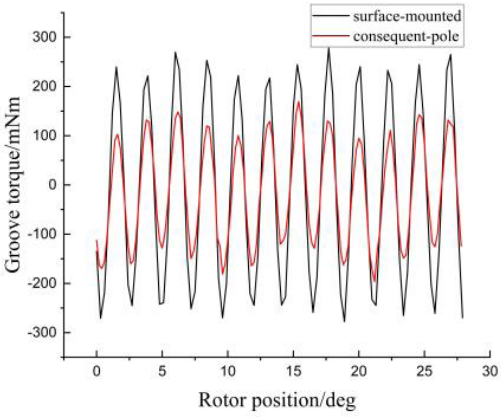

Figure 15. Comparison of output torque.

5. CONCLUSION

In order to solve the problem of high cost of permanent magnet, this paper introduces the consequent-pole based on traditional permanent magnet fault-tolerant vernier machine. In order to ensure the output torque and improve the utilization rate of permanent magnet, the flux-concentrating structure was introduced to optimize the design. Then, the feasibility of the new structure is proved by the analysis of the principle of magnetic field modulation and the finite element simulation experiment. In order to solve the high-dimensional multi-objective optimization problem, the idea of reduced order decoupling was used to transform the multi-parameter high-dimensional problem into low-dimensional optimization problem. The key structural parameters were sensitized by sensitivity analysis, and the multi-objective optimization of the machine was carried out. The optimal optimization effect was obtained, and the effectiveness of the optimization method was verified. Finally, by comparing the no-load air gap flux density, no-load Back-EMF, output torque, cogging torque, and permanent magnet consumption, it is proved that the proposed flux-concentrating consequent-pole permanent magnet fault tolerant vernier rim-driven machine has higher torque density and smaller torque ripple while reducing the consumption of permanent magnet and cost.

ACKNOWLEDGMENT

This work was supported by the National Natural Science Foundation of China under Project 51777024.

REFERENCES

1. Zhi, Y., Y. Ping, O. Wu, B. Fen, et al., "A review of electric motor and control technology for rim-driven thruste," *Transactions of China Electrotechnical Society*, Vol. 37, No. 12, 2949–2960, 2022.
2. Tan, W. Z., X. P. Yan, Z. L. Liu, et al., "Technology development and prospect of shaftless rim-driven propulsion system," *Journal of Wuhan University of Technology (Transportation Science & Engineering)*, Vol. 39, No. 3, 601–605, 2015.
3. Du, D. and K. Yang, "Research on propeller technology development of russian nuclear submarine," *Ship Science and Technology*, Vol. 39, No. 23, 184–187, 2017.
4. Lea, M., D. Thompson, B. V. Blarcom, et al., "Scale model testing of a commercial rim driven propulsor pod," *Journal of Ship Production*, Vol. 19, No. 2, 121–130, 2002.
5. Dine, P. V., "Manufacture of a prototype advanced permanent magnet motor pod," *Journal of Ship Production*, Vol. 19, No. 2, 91–97, 2003.

6. Shen, Y., P. Hu, S. Jin, et al., "Design of novel shaftless Pump-Jet propulsor for multi-purpose long-range and high-speed autonomous underwater vehicle," *IEEE Transactions on Magnetics*, Vol. 52, No. 7, 1–4, 2016.
7. Song, Y., "A new concept pod propulsion technology," *Ship Electric Technology*, Vol. 31, No. 12, 57–59, 2011.
8. Hsieh, M. F., J. H. Chen, Y. H. Yeh, et al., "Integrated design and realization of a hubless rim-driven thruster," *33rd Annual Conference of IEEE Industrial Electronics Society*, 3033–3038, 2007.
9. Varaticeanu, B. D., P. Minciunescu, C. Nicolescu, et al., "Design and validation of a 2.5 kW electric naval propulsion system with rim driven propeller," *2017 Electric Vehicles International Conference (EV)*, 1–5, IEEE, 2017.
10. Kong, B., L.-Z. Xiong, L. Chen, et al., "Research of the model test device design for rim-driven propulsor," *Ship Science and Technology*, No. 12, 163–166, 2017.
11. Zhang, X., J. Liang, M. Qiao, et al., "Design and analysis of propelling motor used in an integrated motor propulsor," *Transactions of China Electrotechnical Society*, Vol. 28, No. 11, 170–175, 2013.
12. Yu, P., J. Zhou, and G. Zhang, "Preliminary design of rim-electric driven propeller and effect factor analysis on cogging torque," *Chinese Journal of Ship Research*, Vol. 13, No. 2, 103–109, 2018.
13. Hu, P., S. Jin, Y. Shen, et al., "Design and multifield coupled analysis of cooling system for PM motor in rim driven propulsor," *Ship Electric Technology*, Vol. 36, No. 3, 28–31, 2016.
14. Qiao, T., "Design and optimization of fault tolerant permanent magnet vernier rim driven machine," Dalian Maritime University, 2022.
15. Cheng, M., H. Wen, P. Han, et al., "Analysis of airgap field modulation principle of simple salient poles," *IEEE Transactions on Industrial Electronics*, Vol. 66, No. 4, 2628–2638, 2019.
16. Li, H., Z. Q. Zhu, and Y. Liu, "Optimal number of flux modulation pole in vernier permanent magnet synchronous machines," *IEEE Transactions on Industry Applications*, Vol. 55, No. 6, 5747–5757, 2019.
17. Liang, Z., Y. Gao, D. Li, et al., "Design of a novel dual flux modulation machine with consequent-pole spoke-array permanent magnets in both stator and rotor," *CES Transactions on Electrical Machines and Systems*, Vol. 2, No. 1, 73–81, 2018.
18. Liu, G., J. Yang, W. Zhao, et al., "Design and analysis of a new fault-tolerant permanent-magnet vernier machine for electric vehicles," *IEEE Transactions on Magnetics*, Vol. 48, No. 11, 4176–4179, 2012.
19. Zhao, W., K. Du, and L. Xu, "Design considerations of fault-tolerant permanent magnet vernier machine," *IEEE Transactions on Industrial Electronics*, Vol. 67, No. 9, 7290–7300, 2020.
20. Chung, S.-U., J.-W. Kim, Y.-D. Chun, et al., "Fractional slot concentrated winding PMSM with consequent pole rotor for a low-speed direct drive: Reduction of rare earth permanent magnet," *IEEE Transactions on Energy Conversion*, Vol. 30, No. 1, 103–109, 2015.
21. Baloch, N., B. Kwon, and Y. Gao, "Low-cost high-torque-density dual-stator consequent-pole permanent magnet vernier machine," *IEEE Transactions on Magnetics*, Vol. 54, No. 11, 8206105, 2018.
22. Li, J. and K. Wang, "Analytical determination of optimal PM-arc ratio of consequent-pole permanent magnet machines," *IEEE/ASME Transactions on Mechatronics*, Vol. 23, No. 5, 2168–2177, 2018.
23. Shi, Y. and L. Jian, "A novel dual-permanent-magnet-excited machine with flux strengthening effect for low-speed large-torque applications," *Energies*, Vol. 11, No. 1, 153, 2018
24. Li, D., R. Qu, J. Li, et al., "Consequent-pole toroidal-winding outer-rotor vernier permanent-magnet machines," *IEEE Transactions on Industry Applications*, Vol. 51, No. 6, 4470–4481, 2015.